



저작자표시-비영리-변경금지 2.0 대한민국

이용자는 아래의 조건을 따르는 경우에 한하여 자유롭게

- 이 저작물을 복제, 배포, 전송, 전시, 공연 및 방송할 수 있습니다.

다음과 같은 조건을 따라야 합니다:



저작자표시. 귀하는 원저작자를 표시하여야 합니다.



비영리. 귀하는 이 저작물을 영리 목적으로 이용할 수 없습니다.



변경금지. 귀하는 이 저작물을 개작, 변형 또는 가공할 수 없습니다.

- 귀하는, 이 저작물의 재이용이나 배포의 경우, 이 저작물에 적용된 이용허락조건을 명확하게 나타내어야 합니다.
- 저작권자로부터 별도의 허가를 받으면 이러한 조건들은 적용되지 않습니다.

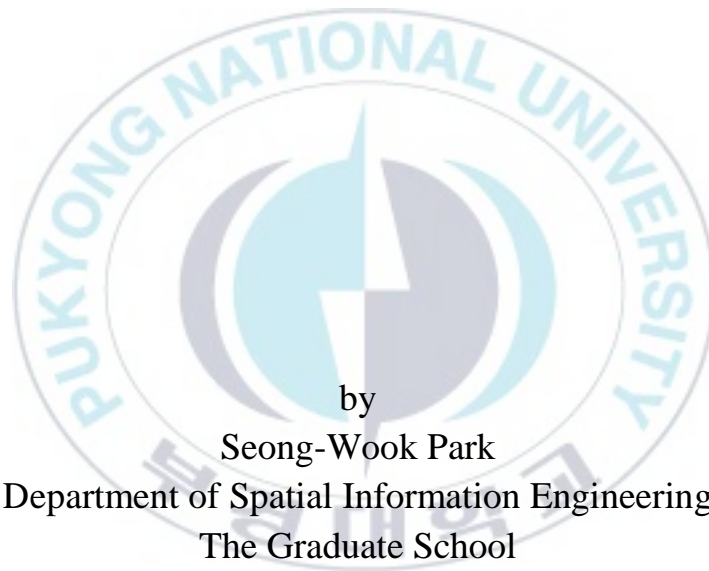
저작권법에 따른 이용자의 권리는 위의 내용에 의하여 영향을 받지 않습니다.

이것은 [이용허락규약\(Legal Code\)](#)을 이해하기 쉽게 요약한 것입니다.

[Disclaimer](#)

Thesis for the Degree of Master of Engineering

Detection of forest fire burned area using Landsat satellite images and Deep learning



by

Seong-Wook Park

Department of Spatial Information Engineering

The Graduate School

Pukyong National University

February 2020

Detection of forest fire burned area using
Landsat satellite images and Deep learning
(Landsat 위성영상과 딥러닝을 이용한
산불 피해지 탐지)

Advisor: Prof. Yang-Won Lee

by
Seong-Wook Park

A thesis submitted in partial fulfillment of the requirements
for the degree of

Master of Engineering
in Department of Spatial Information Engineering,
The Graduate School, Pukyong National University

February 2020

**Detection of forest fire burned area using
Landsat satellite images and Deep learning**

A dissertation
by
Seong-Wook Park

Approved by:

崔哲雄

(Chairman) Prof. Chul-Woong Choi



(Member) Prof. Jin-Soo Kim



(Member) Prof. Yang-Won Lee

February, 2020

CONTENTS

CONTENTS	I
LIST OF FIGURES	II
LIST OF TABLES	IV
LIST OF ACRONYMS	V
ABSTRACT	VII
1. Introduction	1
2. Materials	5
2.1. Satellite Data	5
2.2. Fire Burned Area Data	9
2.3. Input Data and True Label Data	10
3. Methods	11
3.1. Approach Based on Spectral Characteristics of Vegetation	13
3.2. Approach Based on Deep Learning	15
4. Results and Discussion	24
4.1. Prediction of Forest fire Burned Areas Using a DNN classifier	24
4.2. Prediction of Forest fire Burned Areas Using a Semantic Segmentation	27
5. Conclusions	42
6. References	44

LIST OF FIGURES

Figure 1. Overall flow of this study.	12
Figure 2. Structure of U-net model.	19
Figure 3. Example images of data augmentation. The images in the first column are originals and the rest of the images are transformed by data augmentation.	19
Figure 4. R,NIR,G composite images and predict images of DNN classifier.	26
Figure 5. Test images, true label images, prediction images and round images in fold 1 of U-net model.....	31
Figure 6. Test images, true label images, prediction images and round images in fold 2 of U-net model.....	32
Figure 7. Test images, true label images, prediction images and round images in fold 4 of U-net model.....	33
Figure 8. Test images, true label images, prediction images and round images in fold 5 of U-net model.....	34

Figure 9. R, NIR, G composite Images(Top), Images in 3 burn categories
(Red: 'Exactly', Yellow: 'Ambiguous', Black: 'Normal') and U-net
prediction images (Bottom)..... 36

Figure 10. Masking images and histograms for 'Ambiguous' 37



LIST OF TABLES

Table 1. Landsat 5 Thematic Mapper band designations.....	7
Table 2. Landsat 8 Operational Land Imager/Thermal Infrared Sensor(OLI/TIRS) band designations.	8
Table 3. Hyper-parameters list used on U-net model.	23
Table 4. Prediction accuracy of each folds and average accuracy of model in 300 epochs and 10 batch size.	30
Table 5. Confusion matrix to compare the prediction and true values to measure the prediction performance of the model.	39
Table 6. The number of monthly forest fire and calculated PC, POD and FAR values of images used in this study..	41

LIST OF ACRONYMS

UAV	Unmanned Aerial Vehicle
NBR	Normalized Burn Ratio
NDVI	Normalized Difference Vegetation Index
TM	Thematic Mapper
ETM	Enhanced Thematic Mapper
AVHRR	Advanced Very High Resolution Radiometer
dNBR	Difference Normalized Burn Ratio
DL	Deep Learning
ML	Machine Learning
CNN	Convolutional Neural Network
OLI	Operational Land Imager
TIRS	Thermal Infrared Sensor
FWI	Fire Withering Index
SLC	Scan Line Corrector
VNIR	Visible and near-infrared
USGS	United States Geological Survey

DNN	deep neural network
ANN	Artificial Neural Network
FCL	Fully Connected Layer
ILSVRC	Large Scale Visual Recognition Challenge
FCN	Fully Convolutional Network
CE	Cross Entropy
BCE	Binary Cross Entropy
ADAM	Adaptive Moment Estimation
SGD	Stochastic Gradient Descent
RMSprop	Root Mean Square Propagation
ReLU	Rectified Linear Unit
PC	Proportion Correct
POD	Probability of Detection
FAR	False Alarm Ratio
DEM	Digital Elevation Model

Landsat 위성영상과 딥러닝을 이용한 산불 피해지 탐지

박 성 옥

부경대학교 대학원 공간정보시스템공학전공

요 약

우리나라는 약 70%가 산악지역으로 이루어져 있어 산불 발생 시 그 피해가 막대하다. 이러한 지형적인 특징으로 인해 사람의 접근이 어렵고, 피해 면적이 광범위하기 때문에 원격탐사 기법의 필요성이 증대되고있다. 위성 영상 및 항공 영상과 식생의 분광 특성을 활용하여 개발 된 지수들을 이용해 산림의 피해 유무를 분류하고, 피해 정도 및 식생의 회복 정보 등을 탐지하는 연구들은 많이 선행되어 왔다. 하지만 이러한 지수들을 활용한 피해지 탐지 관련 선행연구들은 피해지를 효과적으로 표현하기 위해 연구자의 주관이 많이 반영이 되고, 탐지하고자 하는 지역 및 계절적 특성, 영상의 화질 차이 문제 등으로 인해 임계치를 조정해야하는 한계점이 존재한다. 이에 본 연구에서는 최근 빠른 속도로 발전하고 있는 딥러닝 영상 인식 기술을 원격탐사 기술에 적용하여 분광 특성 기반의 피해지 탐지 연구들의 한계점을 보완하고, 새로운 산불 피해지 영상으로부터 연구자의 주관이 개입되지 않고 신속히 산불 피해지를 탐지할 수 있는 모델을 구축 및 최적화하고자 하였다. 이를 위해 Landsat 5 TM (Thematic Mapper), Landsat 8 OLI/TIRS (Operational Land Imager / Thermal Infrared Sensor) 위성 영상과 산불 피해지 분석에 주로 사용되는 NBR, NDVI, FWI 지수를 딥러닝 모델의 입력자료로 활용하여 산불 피해지를 탐지하였다. 피해지 탐지를 위해 활용한 딥러닝 모델은 Deep Neural Network(DNN) Classifier 와 Semantic Segmentation 기법 중 U-net 모델을 활용하였다. DNN classifier 와 U-net 각각 약 89%, 93%의 높은 예측 정확도를 보였으며, 본 연구를 통해 산림 재해에 대해 딥러닝의 적용이 가능함을 검증하였다.

1. Introduction

Recently, the damage caused by abnormal weather and disasters has been increasing rapidly around the world, especially in Korea, as about 70 percent of the country is made up of mountainous areas, causing huge damage in case of forest fire. Due to this geographical feature of Korea, the need for remote sensing is increasing because it is difficult for human to access and the area of damage is extensive [Song et al., 2006]. Recently, GoSeong-Sokcho and GangNeung-DongHae, in April 2019, has declared state of disaster of massive fires causing environmental and economic damage [Park et al., 2019]. The existing research about detect to damage areas was basically conducted through field or air observation, which has the disadvantage of having a large manpower and time-consuming. Considering these economic costs and the accessibility of field observations, the benefits of remote sensing can be seen as significant [Won et al., 2001], and it is more efficient to use them than field observations to investigate damage from forest fire and monitoring the recovery process of vegetation, and expedite the forest recovery plan [Kang et al., 2010; Ryu et al., 2018]. Also, forest fire caused by artificial and natural fires have a very important effects on the environment, human

life, and property [Sunar and Özkan, 2001], it is necessary to find ways to quickly identify the area and extent of forest fire in order to keep them sustainable [Kang et al., 2010]. Many research has been conducted on how to classification forest damage by using developed indices using different aviation platforms such as Landsat, Sentinel, and Unmanned Aerial Vehicle (UAV) and other factors to detect forest fire damage by utilizing satellite images such as damage degree and information on the recovery of vegetation. Normalized Burn Ratio (NBR) and Normalized Difference Vegetation Index (NDVI) among indices using the spectral traits of vegetation are mainly used in forest damage detection research. Won et al. [2007] calculated the area and damage intensity of forest fire using Landsat TM and Landsat ETM+ images and dNBR (Difference NBR), which is the difference between NBR before and after forest fire damage, and assessed damage to forest fire and the damage strength of the affected areas to quantify the rate of recovery.

In addition to dNBR, there are preceding studies on the frequency of forest fire, detection of damaged areas, and measurement of damage intensity using NDVI [Lutz et al., 2011; Nararro et al., 2017; Lee et al., 2017]. However, there are limitations that must be manually adjusted because preceding studies related to damage detection is highly reflective of the researchers in order to effectively express the damaged areas, and

the regional and seasonal traits that they want to detect, and the differences in image quality are different [Park et al., 2019; Kang et al., 2010; Lee et al., 2017; Turker and San, 2003; Park and Lee, 2019]. Accordingly, advance research is being conducted based on artificial intelligence (AI) that allows computers to observe faster and more accurate location and area of damage on their own. In addition, recent research using Deep Learning (DL), a more advanced form of traditional machine learning, is being conducted due to the amount of data and the development of computer hardware [Long et al., 2015; Song et al., 2018; Kussul et al., 2017]. Zhang et al. [2015] used UAV images and Deep Convolutional Neural Network (CNN) to detect forest fire in RGB forest fire images, Kim et al. [2016] used UAV optical sensors and deep learning to develop a platform for disaster recognition and response to detect forest fire damage detection and prevent secondary damage through the Smart-eye platform, a forest fire monitoring technology. However, most of the preceding studies using deep learning and satellite images are mainly focused on detecting and classifying land cover changes using high-resolution images [Song et al., 2018; Kussul et al., 2017; Zhang et al., 2015], preceding studies that detected forest fire damage using satellite imagery and deep learning are not sufficient.

Therefore, in this study, we complement the limitations of spectral character-based damage detection studies using remote sensing and deep learning, and to construct and optimize an artificial intelligence-based forest fire damage detection model that does not involve the researcher's subjectivity from the new forest fire damage image.

For this study, we calculated NBR, NDVI, and Fire Withering Index (FWI) [Park et al., 2019], which are mainly used for forest fire damage research from Landsat 5 TM (Thematic Mapper) and Landsat 8 OLI/TIRS (Operational Land Imager / Thermal Infrared Sensor) images, and these indices used as input data of deep learning model to detect forest fire damage more accurately and effectively.

2. Materials

2.1. Satellite Data

In this study, we used Landsat 5 TM and Landsat 8 OLI/TIRS satellite images provided by the United States Geological Survey (USGS). Earth-explorer (<https://earthexplorer.usgs.gov>) provides images such as Landsat, Sentinel, AVHRR (Advanced Very High Resolution Radiometer) and in Landsat, calibrated level-2 surface reflectance images are available in all bands except panchromatic and thermal bands. For Landsat 4-5 TM and Landsat 7 ETM+, Surface Reflectance is calculated using the Landsat Ecosystem Disturbance Adaptive Processing System (LEDAPS) algorithm [Masek et al., 2006], and Landsat 8 OLI/TIRS is calculated through Land Surface Reflectance Code (LaSRC) [Vermote et al., 2016].

Landsat 5 TM is a satellite launched in 1984 for earth observation, and is equipped with a Thematic Mapper (TM) sensor. The visible band (Band 1 to Band 5 and Band 7) of the Landsat 5 TM has a spatial resolution of 30m and 120m for the thermal infrared band (Band 6) [Won et al., 2007] (Table 1). In the case of Landsat 7 Enhanced Thematic Mapper (ETM) +, there are many noises in the affected area due to Scan Line Corrector

(SLC)-off problem, and there is no Landsat 5 TM data since 2012, therefore we used Landsat 8 OLI/TIRS images.

Landsat 8 OLI/TIRS is equipped with two sensors, OLI and TIRS, to provide images in the visible and near-infrared (VNIR) and thermal infrared (TIR) bands. The spatial resolution is the same as the Landsat 5 TM at 30m (visible band), and data obtained from OLI and TIRS sensors improved signal-to-noise performance compared to other Landsat series images, making it easier to analyze the condition and traits of the surface [Roy et al., 2014].

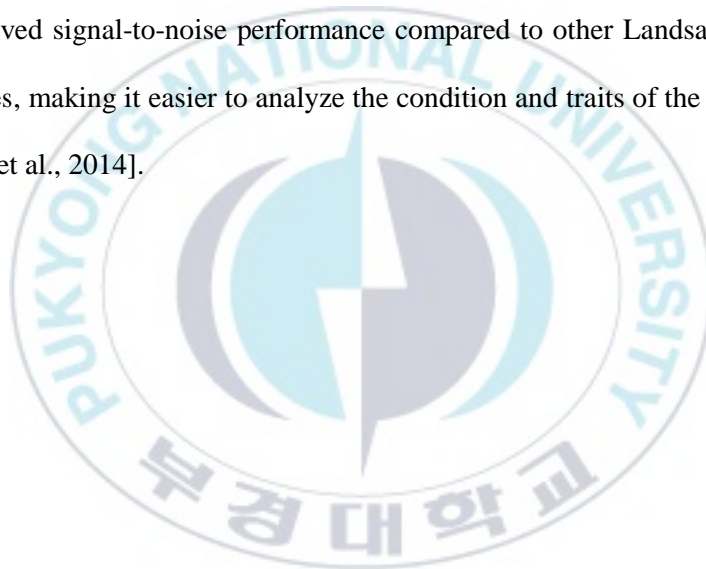


Table 1. Landsat 5 Thematic Mapper band designations

Landsat 5

Band description	Wavelength(μm)	Resolution(m)
Band1(Blue)	0.45-0.52	30
Band2(Green)	0.52-0.60	30
Band3(Red)	0.63-0.69	30
Band4(NIR)	0.76-0.90	30
Band5(SWIR1)	1.55-1.75	30
Band6(Thermal)	10.40-12.50	120
Band7(SWIR2)	2.08-2.35	30

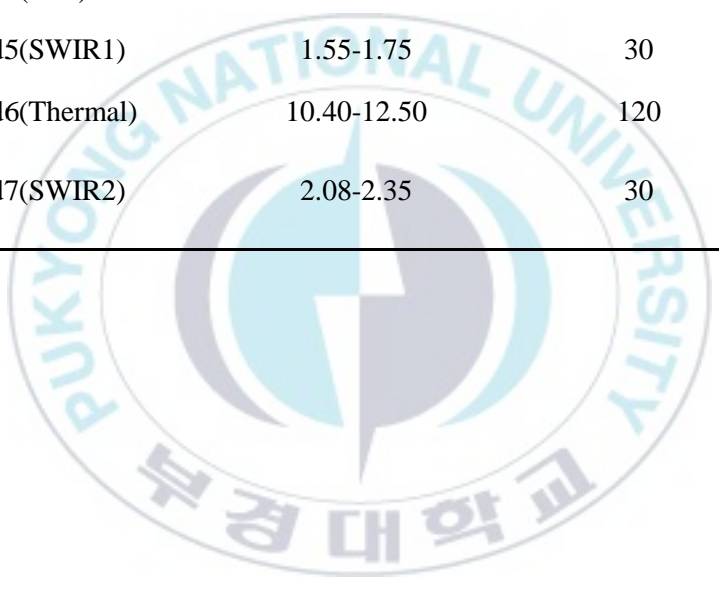


Table 2. Landsat 8 Operational Land Imager/Thermal Infrared Sensor(OLI/TIRS) band designations

Landsat 8

Band Description	Wavelength (μm)	Resolution(m)
Band1 (Coastal aerosol)	0.43-0.45	30
Band2 (Blue)	0.45-0.51	30
Band3 (Green)	0.53-0.59	30
Band4 (Red)	0.64-0.67	30
Band5 (NIR)	0.85-0.88	30
Band6 (SWIR1)	1.57-1.65	30
Band7 (SWIR2)	2.11-2.29	30
Band8 (Panchromatic)	0.50-0.68	15
Band9 (Cirrus)	1.36-1.38	30
Band10 (Thermal Infrared 1)	10.60-11.19	100
Band11(Thermal Infrared 2)	11.50-12.51	100

2.2. Forest fire Burned Area Data

For the forest fire damage data used in this study, the area of damage over 10 hectares (ha) was selected for 16 years (2003 – 2018) by referring to the ‘Forest fire Damage Register’ provided by the Korea Forest Service. If the size of the damage area is too small, the error rate may increase due to the influence of the surrounding pixels during the model learning process. As a result, there were 107 cases of damage of more than 10 hectares in total 6,910 cases of damage in the ‘Forest fire Damage Register’, and 48 images were obtained. It was difficult to obtain a large number of images because of the limitations in obtaining images due to the presence of the problem of location discrimination due to the influence of shadows in clouds and mountain ranges or lack of images in the areas.

2.3. Input Data and Label Data

In the case of deep learning, the number of input images and true labels used for learning are important [Najafabadi et al ., 2015], In recent deep learning research, deep learning models can be trained without the need for label creation because there is dataset with large numbers of images and true labels such as ImageNet, MS COCO, and MNIST [Najafabadi et al ., 2015; LeCun et al., 2015], but this study needs to collect input image and create true labels because there is no satellite image and true label for forest fire damage. Therefore, the size of the input image to be used in this study was set to 96 x 96 to reduce errors caused by the surrounding pixel values around the forest fire, and only the parts of the damaged areas were clipped from the entire image.

In the case of the true label, since the true label for deep learning about forest fire damage is not established, we have determined the area of damage by referring to RGB true color images and R, NIR and G composite images for 48 areas. Using the Qgis software, we created a polygon map of the damaged area and the true label consisting of 0 and 1 values (one-hot encoding) was created through rasterizing.

3. Methods

In this study, we used indices using the spectral traits of vegetation as input data for deep learning to verify the applicability of deep learning in the field of remote sensing and the availability of detection of forest fire damage areas, and to establish and optimize a fast and accurate artificial intelligence-based model for detecting forest fire damage from images of new forest fire.

The overall study flow chart is as shown in Figure 1. Red, Green, Near Infrared bands of three visible bands and indices(NBR, NDVI, FWI) created by the spectral traits of vegetation were used as input data for deep learning models, and we used DNN Classifier and Semantic Segmentation to detect, compare and analyze forest fire damage areas.

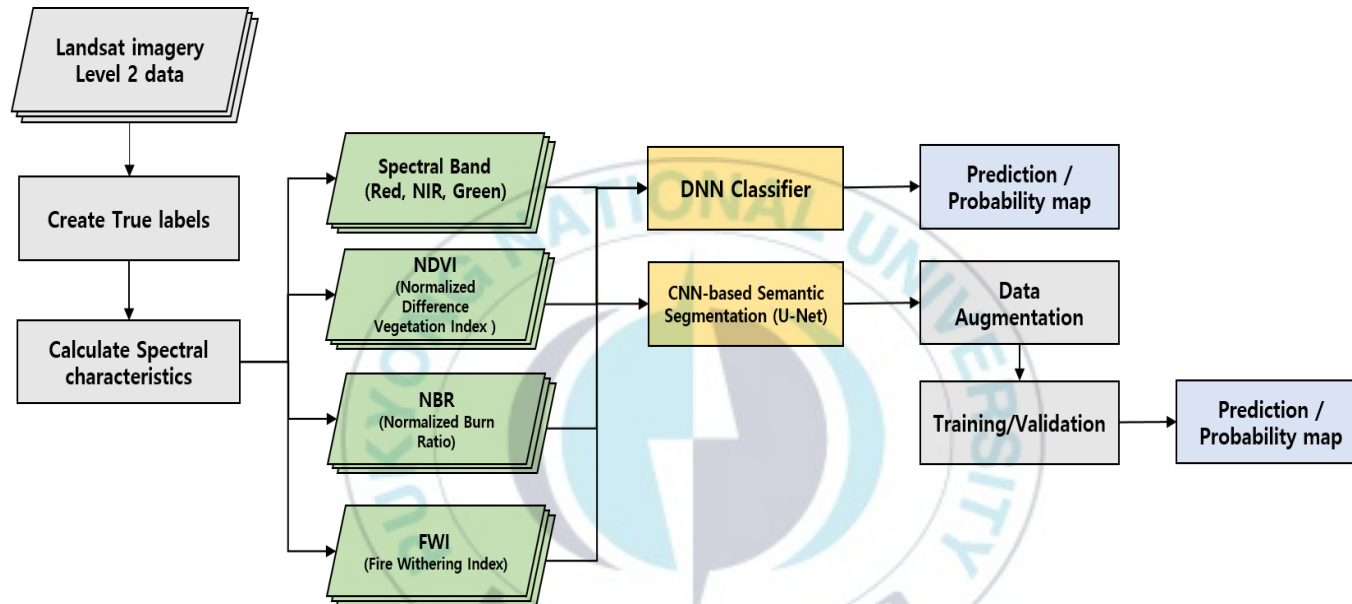


Figure 1. Overall flow of this study.

3.1. Approach Based on Spectral Characteristics of Vegetation

Healthy vegetation mainly absorbs the red band and reflects the green band and near infrared band, but the damaged vegetation exhibits the opposite spectral traits, so there are many indices and preceding studies using contrasting spectral traits of damaged forest and normal [Kumar et al., 2002]. In this study, we used NBR, NDVI, and FWI.

NBR is an index that is a formalized form using difference and the sum of near-infrared and mid-infrared reflectance. Since the moisture in the vegetation has a high absorption rate in the mid-infrared band, the higher the moisture content, the lower the reflectance of the mid-infrared band. Therefore, healthy forests have high NBR due to low reflectance of mid-infrared band, while damaged forests have relatively low NBR due to high reflectance of mid-infrared reflectance [Won et al., 2007; Miller and Thode, 2007]. We used Band 4 and Band 7 for Landsat 5 TM (Equations 1), and Band 5 and Band 7 for Landsat 8 OLI/TIRS to calculate the NBR.

$$\text{NBR} = \frac{\text{Band 4} - \text{Band 7}}{\text{Band 4} + \text{band 7}} \quad (1)$$

NDVI is calculated using the traits that the difference in vegetation reflectance is large in red band and near infrared band, it is mainly used to identify the situation of vegetation distribution. NDVI has a value between -1 and 1, and the higher the value of healthy forests, the lower the value if there is damage or little vegetation [Lee et al., 2012]. We used Band 3 and Band 4 for Landsat 5 TM (Equations 2), and Band 4 and Band 5 for Landsat 8 OLI/TIRS to calculate the NDVI.

$$\text{NDVI} = \frac{\text{Band 4} - \text{Band 3}}{\text{Band 4} + \text{Band 3}} \quad (2)$$

FWI is an index indicating the damage by weighted band reflectance, using the red, green, near-infrared bands among several combinations to best represent forest fire damage, and using the traits of high reflectance of the near-infrared band in healthy forests. Park and Lee [2019] developed and applied FWI to large forest fire in GoSeong-SokCho and GangNeung-DongHae in April 2019 to detect and extract the area of damage quickly. We used Band 2, Band 3 and Band 4 for Landsat 5 TM (Equations 3), and Band 3, Band 4 and Band 5 for Landsat 8 OLI/TIRS to calculate the FWI.

$$\text{FWI} = (0.3 * \text{Band 3}) + (0.6 * \text{Band 4}) + (0.1 * \text{Band 2}) \quad (3)$$

3.2. Approach Based on Deep Learning

Recently, as the use of high-performance computers has become more common due to the development of hardware along with the utilization of big data, the use and interest of DL, a more advanced form of ML, has been increasing [Szegedy et al., 2013]. Even with deep network layers, the time required for training is reduced and the accuracy of DL models is gradually increasing [LeCun et al., 2015]. Typical DL models include Deep Neural Network(DNN) and Convolutional Neural Network(CNN).

DNN is a deeper model of the Artificial Neural Network(ANN), which consists of several hidden layers between the input and output layers [Bengio et al., 2013]. It is a DL model that can improve the problems of classical machine learning and ANN and performs well in object detection as well as classification [Szegedy et al., 2013]. DL uses several techniques to prevent overfitting in which the model only describes some specific data in the process of testing the model, and increase accuracy in optimizing models such as back-propagation algorithms, activation functions, and drop-out, etc [Long et al., 2015; Brownlee, 2018; Ronneberger et al., 2015].

CNN is a type of neural network that is being studied a lot in various image processing and computer vision fields, such as image recognition

by computer and extracting high levels of abstracted information from them, or drawing new pictures [Kim et al., 2014]. As shown in Figure 2, the CNN's structure has repeatedly piled up a convolution layer that performs a convolution operation, a filter operation used in image processing, in front of the existing ANN, and the structure can be divided into a part that extracts the features of an image using a filter and a Fully Connected Layer(FCN) that classifies the class [LeCun et al., 2015]. Many CNN models (AlexNet [Krizhevsky et al., 2012], VGGNet [Simonyan et al., 2014], GoogLeNet [Szegedy et al., 2015], and ResNet [He et al., 2016]) have been demonstrated and are being studied to improve performance at the ILSVRC (Large Scale Visual Recognition Challenge Challenge) competition, which gives large sets of images such as image recognition and classification. However, these CNN models have computational problems at the FCL, or the problem of receiving only fixed-size inputs, and the problem of losing the location and spatial information for the input images because the three-dimensional input is converted to one-dimensional vector form as it passes through the FCL [LeCun et al., 2015]. This can be seen as a limitation for use in remote sensing where location and spatial information is important [Song et al., 2018]. Therefore, this study used Semantic Segmentation based on CNN.

Semantic Segmentation is an image recognition technique applied to pixel-wise classification unlike CNN, which categorizes images as a whole [LeCun et al., 2015; Noh et al., 2015]. Whereas CNN classifies what a target is for an image, Semantic Segmentation classifies it into pixels, allowing it to include all information about what the target is and where it is located [Noh et al., 2015].

Semantic Segmentation considers CNN's fully connected layer to be 1x1 convolution, which allows the entire structure to perform convolution operations, thereby maintaining location information and not limiting input images. [LeCun et al., 2015]. The U-net used in this study is a representative model of Semantic Segmentation that has demonstrated effective performance in discriminating cell boundaries and cancer cells in the field of medical image segmentation [Ronneberger et al., 2015]. In the field of medical image segmentation, the objective is to distinguish between normal and abnormal pixels, so we judged that U-net could be applied to the field of remote sensing.

U-net is a model designed with Contracting path and Expanding path. Contracting path is the process of extracting features while reducing the size of the input image, and Expanding path is the process of restoring to the original image size while preventing loss of location information [Ronneberger et al., 2015]. When up-sampling to restore the image size in

the expanding path, U-net used copy and crop, which refers to the feature of the contracting path as shown in the gray line in Figure 2, to obtain more accurate localization, and Data augmentation has shown good performance in biomedical segmentation applications even with a small number of training samples [Ronneberger et al., 2015].

Data augmentation techniques are used by many studies to increase the number of data learned by inverting, shifting, and distorting the input image. Many studies have been used to improve the stability and accuracy of the learning model, and to prevent overfitting [Kim et al., 2016; Ronneberger et al., 2015; Krizhevsky et al., 2012]. In this study, data augmentation was used because the number of training samples required for training was not large (Figure 3).

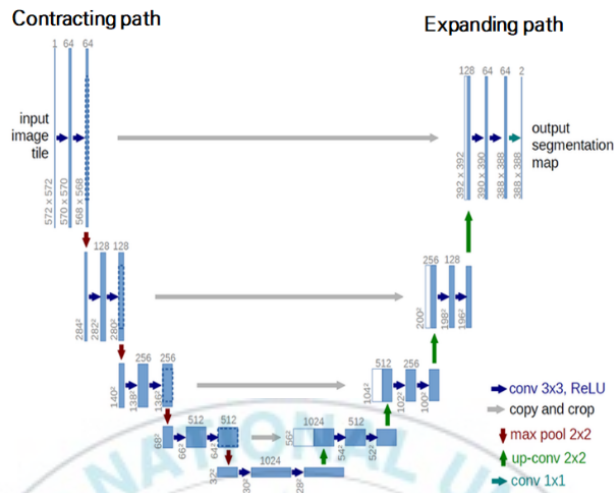


Figure 2. Structure of U-net model [Ronneberger et al., 2015].

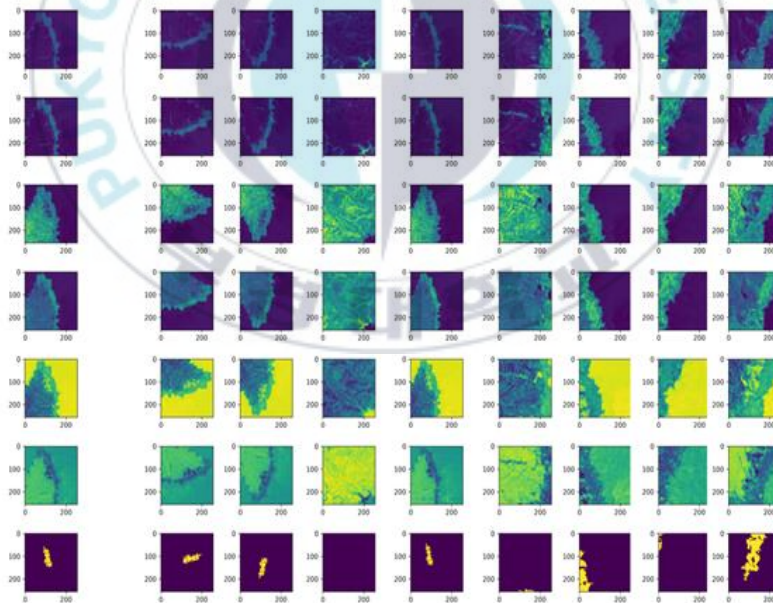


Figure 3. Example images of data augmentation. The images in the first column are originals and the rest of the images are transformed by data augmentation.

The loss function of the model was Binary Cross Entropy(BCE). In general, Squared Sum Error(SSE) is used for regression, and Cross Entropy(CE) is mainly used for classification. As shown in Equation 4, \log is the natural logarithm base $e(\log_e)$, y_i is the prediction result, and t_i is the true label. In this case, t_i shall have a one-hot encoding form in which the correct answer has a value of 1 and all the rest have 0 [Pappagari et al., 2018]. BCE is a special form of CE, and if one probability is p , the other probability is a function of the two patterns in which one probability is $1-p$. In Equation 5, i denoted a sample number, y_i denoted output data(0 to 1) of the i -th sample class k , and t_i denoted a true label (0 or 1) of the i -th sample class k [Pappagari et al., 2018; Wang et al., 2017]. Because of the effects of negative symbols, the higher the number of matched samples, the lower the overall error, since the output data and true label (e.g., forest fire 1, normal 0) are allowed to have a maximum value rather than the maximum value when fully matched.

$$CE(t, y) = - \sum_{i=1}^N t_i \cdot \log(y_i) \quad (4)$$

$$BCE(t, y) = - \frac{1}{N} \sum_{i=1}^N t_i \cdot \log(y_i) + (1 - t_i) \cdot \log(1 - y_i) \quad (5)$$

We used Adaptive Moment Estimate(Adam) as an optimizer. In DL, the optimizer is a neural network optimization method that allows the speed-up and stabilizes learning by updating weight values in a direction that minimizes the resulting of loss function values [Lim et al., 2017]. Among them, Adam is currently the most commonly used optimizer in DL that combines Momentum, which complements the shortcomings of the Stochastic Gradient Descent (SGD), and Root Mean Square Propagation (RMSprop), which prevents learning rate decay, by only reflecting new gradient information [Lim et al., 2017; Kingma and Ba, 2014].

We used Rectified Linear Unit (ReLU) as an activation function. The ReLU is a function designed to compensate for the drawback of gradient vanishing problem when passing through layers when performing back-propagation, which is a disadvantage of Sigmoid function. If the input value is less than 0, it outputs 0, and if it is greater than 0, the input value is output as it is [Krizhevsky et al., 2012; Nair and Hinton, 2010].

$$\text{ReLU}, f = \begin{cases} x < 0, f(x) = 0 \\ x \geq 0, f(x) = x \end{cases} \quad (6)$$

In this study, ReLU was used until before the last convolution layer of the U-net model, and since the last layer used Sigmoid function, the predicted images produced as a heat map image with probability values in

the range of 0 to 1. The hyper-parameters used in the study are shown in Table3.



Table 3. Hyper-parameters list used on U-net model.

U-net model hyper-parameter	
Input images	960 (train + val + test)
Input size	96 x 96
Layers	R,NIR,G,FWI,NBR,NDVI
Spatial Resolution (m)	30
Epochs	300
batch size	10
Loss function	Binary cross entropy
Optimizer	Adam(Adaptive Moment Estimation)
Activation function	ReLU (Rectified Linear Unit) / Sigmoid (Last layer)
Output	Probability Map (0~1)

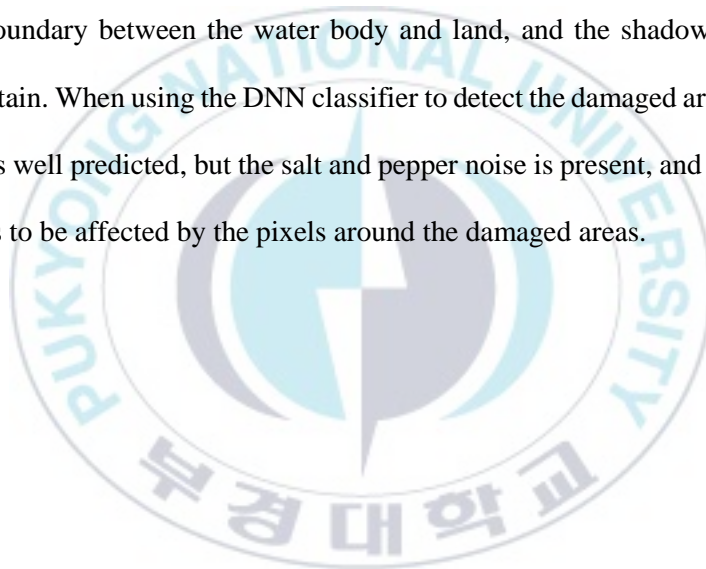
4. Results and Discussion

4.1. DNN Classifier

The spectral traits-based approach can effectively explain forest disaster phenomena, but has limitations in that the threshold setting must be made empirically and manually [Park et al., 2019; Kang et al., 2010; Lee et al., 2017; Truker and San, 2003]. Therefore, we used the spectral traits-based information as input data for DL, thereby enhanced the advantages and complemented the disadvantages of the spectral traits-based approach.

In this study, we tried to detect the damaged areas by constructing a DNN classifier using the R software's h2o library. 'H2O' library is a Java-based open source platform for machine learning, deep learning deployment and analysis of big data [h2o]. We created a matchup data (approximately 440,000 pixels) that arranged the pixel values of all layers (R, NIR, G, NBR, FWI and NDVI) of the images used as input data for DNN classifier. The number of training (epochs) consisted of 1000 times and the number of hidden layers was 200 x 200. We also divided the data into 6 folds to predict all 48 damaged areas and built a dataset to predict 8 images for each fold. As a result of the DNN classifier test, the average

prediction accuracy was 89.72%, we generated the predicted images by rasterizing the pixel values of each image predicted by DNN classifier. The prediction images showed that the predicted damaged areas were very similar to the R, NIR and G composite images (Figure 4). However, it can be seen that there is a tendency to make false alarm about the area having the similar pixel value as the pixel of the damaged areas such as the urban, the boundary between the water body and land, and the shadow of the mountain. When using the DNN classifier to detect the damaged areas, the area is well predicted, but the salt and pepper noise is present, and since it seems to be affected by the pixels around the damaged areas.



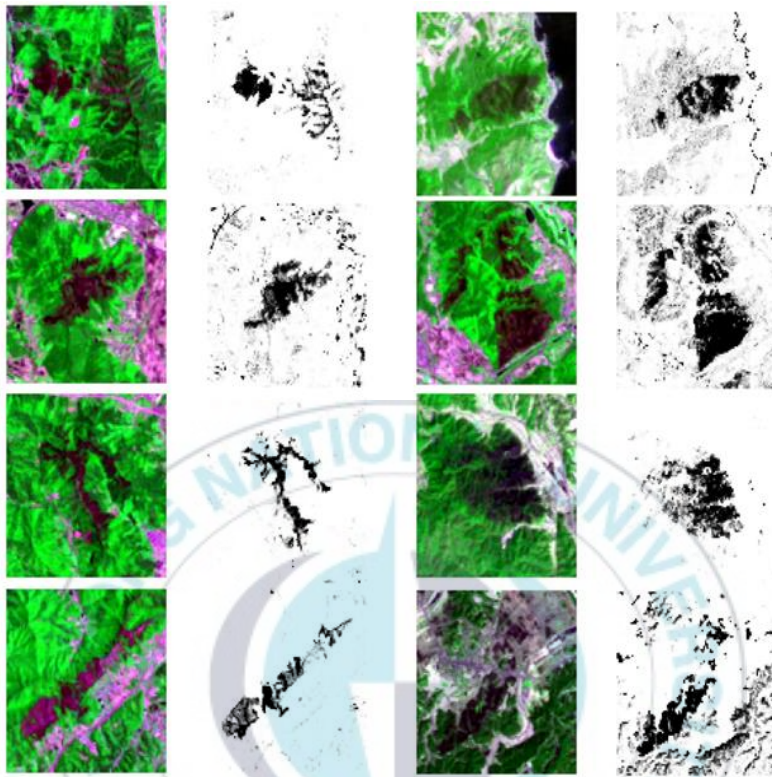


Figure 4. R, NIR, G composite images and predict images of DNN classifier.

4.2. Prediction of Forest fire Burned Areas Using a Semantic Segmentation

In order to use the U-net model, we augmented 48 original images to 960 through data augmentation, and then constructed the dataset with 800 training data, 80 validation data, and 80 test data. And cross validation was performed to select the model's optimal hyper-parameter and to verify the model's generalization capability through various test sets. Model training and validation under various conditions, such as learning epochs, learning rate and batch size, resulted in the highest accuracy and low loss value when learning epochs 300, learning rate 0.001, batch size 10.

We divided the dataset into 12 folds to ensure that the data of the training, validation and test sets do not overlap each other, and computed the average prediction accuracy by constructing the test sets for each fold differently. In addition, if Normalization or Standardization is applied to the input data during the DL process, the distribution of data values is set to 0 to 1 or -1 to 1 so that the model can be trained stably and the learning speed is improved [Yang et al., 2015]. Thus, through data standardization (Equation 6), we transformed the input data into a standard normal distribution with a mean of 0 and a standard deviation of 1 [Mesnil et al., 2011].

$$X_s = \frac{X-\mu}{\sigma} \quad (6)$$

$$\text{Where } \mu = \frac{1}{n} \sum_{i=1}^n x_i \text{ and } \sigma = \sqrt{\frac{1}{n-1} \sum_{i=1}^n (x_i - \mu)^2} \quad (1)$$

The test result of the U-net model was 0.926, achieving high average prediction accuracy. Compared with the DNN classifier prediction result, the U-net model shows that the damaged area is clearly revealed, and the ratio of the surrounding false alarm such as salt and pepper effect is also reduced.

For a convenient comparison between the predicted image and the true label, the pixel values of the predicted image were rounded to create a round image expressed as 0 and 1 and the true label looked very similar when compared (Figure 5 – Figure 8). However, like the DNN classifier, there is a problem in which the non-damaged area is false alarm as the damaged area when the damage value and the pixel value distribution are similar, such as roads, shadows, and urban areas. Also, the prediction accuracy was about 3% higher for U-net model. Therefore, it is judged that it is highly useful for the rapid detection of forest fire damaged areas and extracting the estimated areas.

In the case of fold 4, the accuracy is lower than other folds (Table 4), which indicates that the accuracy is lowered because an error occurs in the area where the true label can't show the damage detail. Although the accuracy is low, it is judged that the accuracy is lowered because an error occurs in the area where the true label can't the damage detail. If the true label is made as detailed as possible in the future, the prediction accuracy will be better.



Table 4. Prediction accuracy of each folds and average accuracy of model in 300 epochs and 10 batch size.

	Accuracy
Fold 1	0.871
Fold 2	0.961
Fold 3	0.883
Fold 4	0.851
Fold 5	0.932
Fold 6	0.929
Fold 7	0.940
Fold 8	0.923
Fold 9	0.968
Fold 10	0.948
Fold 11	0.951
Fold 12	0.949
Average	0.926

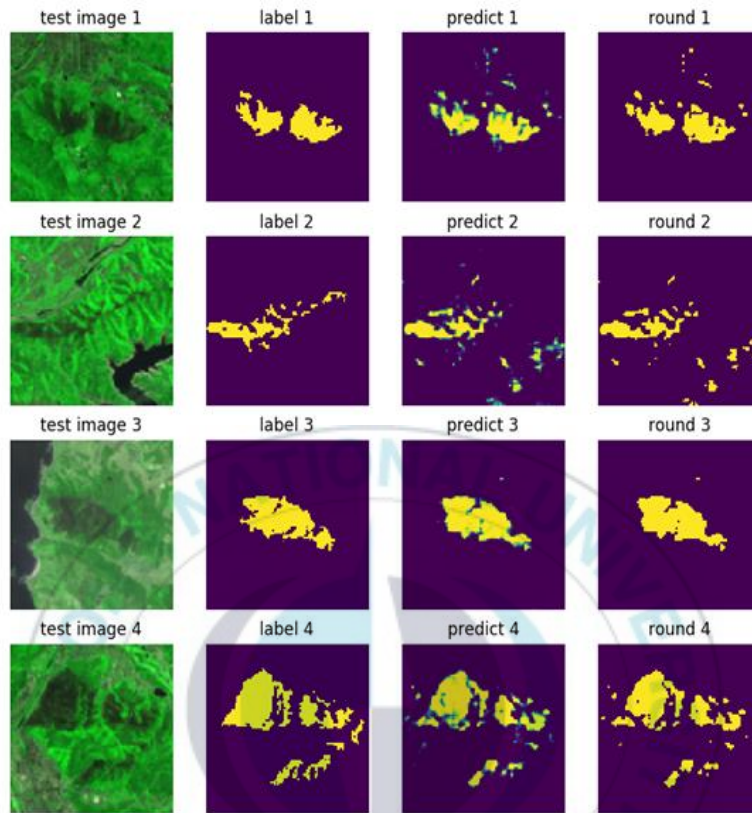


Figure 5. Test images, true label images, prediction images and round images in fold 1 of U-net model

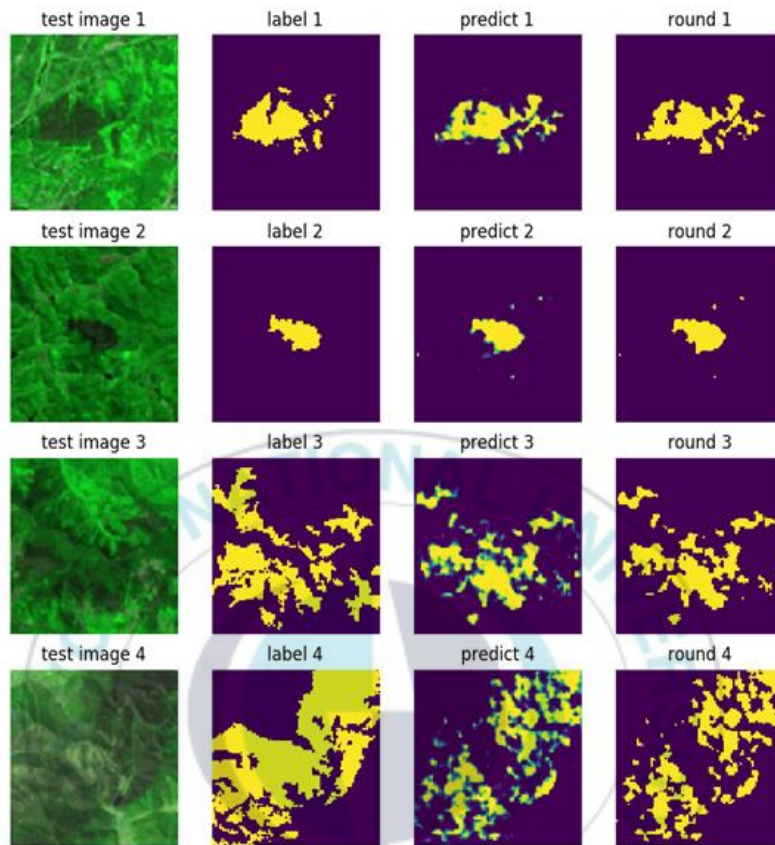


Figure 6. Test images, true label images, prediction images and round images in fold 2 of U-net model

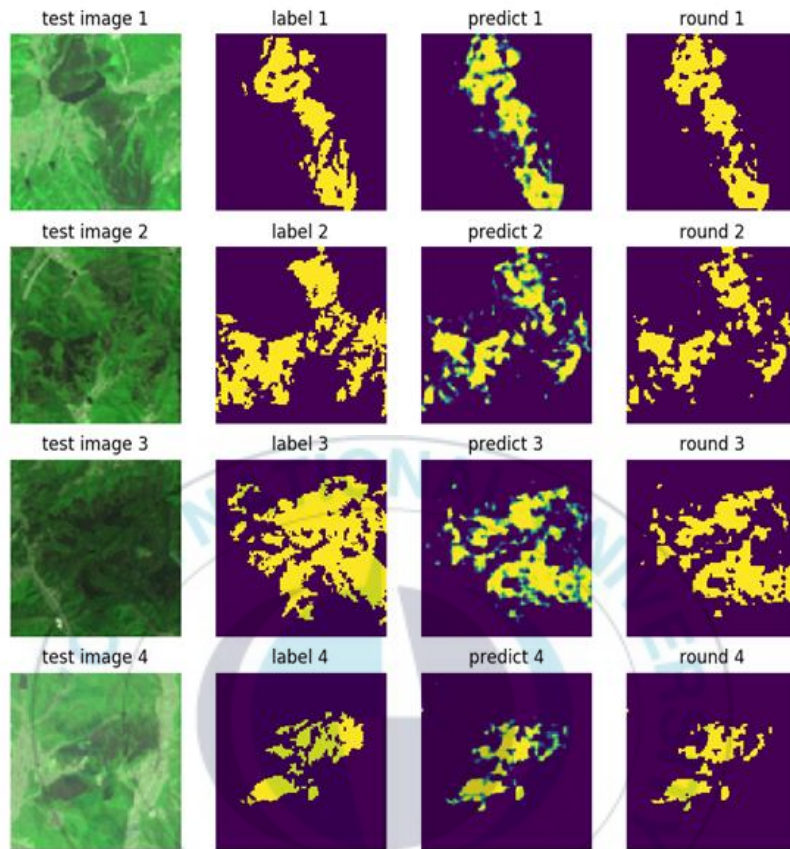


Figure 7. Test images, true label images, prediction images and round images in fold 4 of U-net model

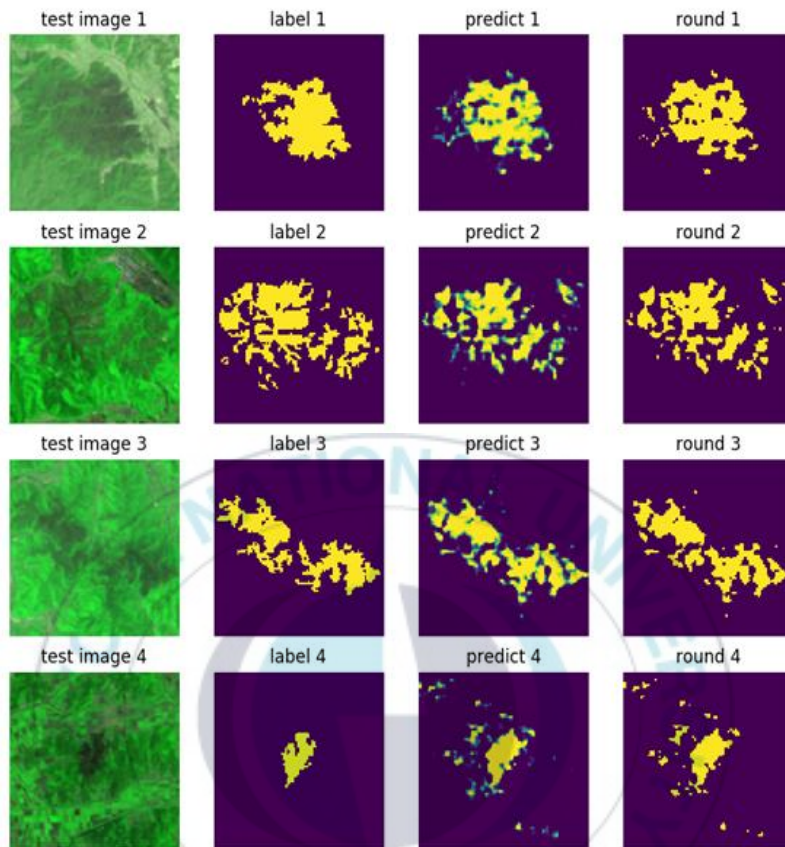


Figure 8. Test images, true label images, prediction images and round images in fold 5 of U-net model

We found that there was a part of the labeling process that was difficult to judge clearly between damaged area and un-damaged area. Therefore, in order to know whether these difficult parts affect the prediction accuracy, we selected four areas of difficulty during the creating true labels and divided forest fire severity into three categories ('Exactly', 'Ambiguous', 'Normal'). And compared them to the U-net prediction images (Figure 9). The distribution of pixel values by masking only the areas identified as "Ambiguous" showed the highest ratio of pixels of over 0 and less than 0.1 in all four regions (Figure 10). This shows even if ambiguous parts are included in the process of creating the true label, it is more likely to be predicted as a non-damaged, and the proportion of areas where the model predicted as a damaged area from those corresponding to 'Ambiguous' was low.

Thus, we found that the true labels for forest fire damage were generated manually, but the ambiguity was not enough to affect prediction accuracy. This study has shown that even with the limitation of training with a small number of samples, U-net's prediction result can predict the area similar to forest fire damaged areas. And if more samples are made and utilized in the future, the model is expected to improve with higher accuracy.

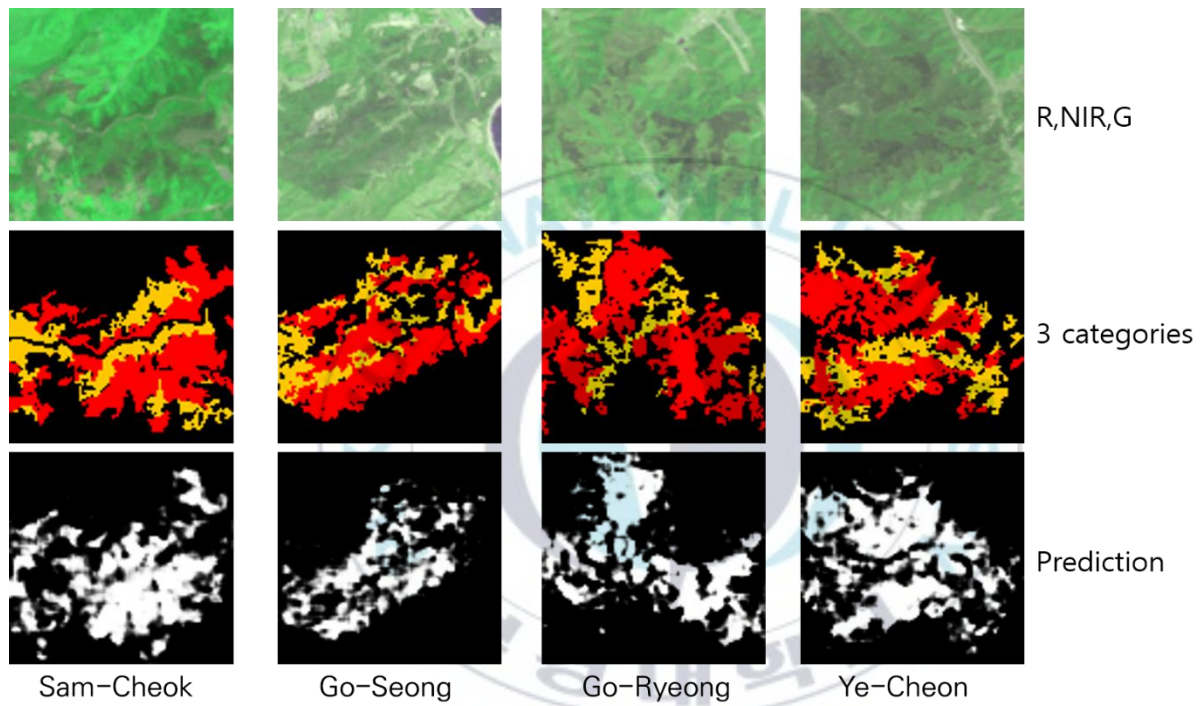
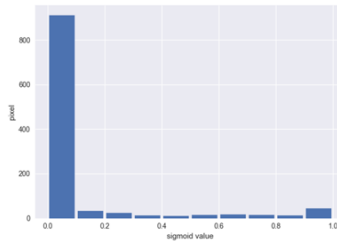
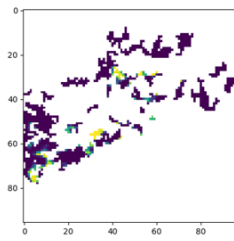
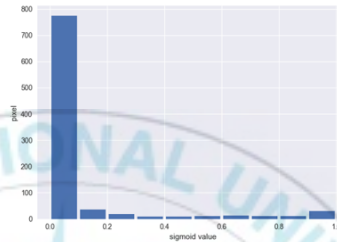
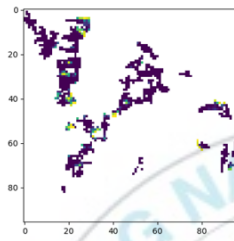


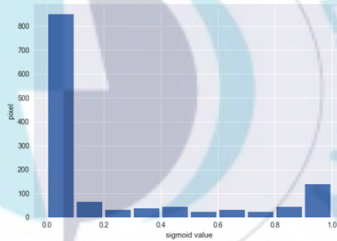
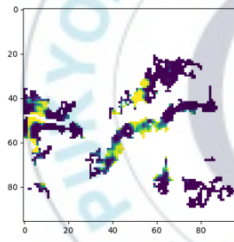
Figure 6. R,NIR,G composite Images(Top), Images in 3 burn categories(Red: 'Exactly', Yellow : 'Ambiguous', Black: 'Normal') and U-net prediction images (Bottom)



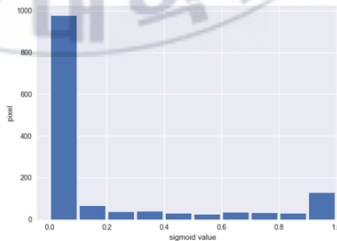
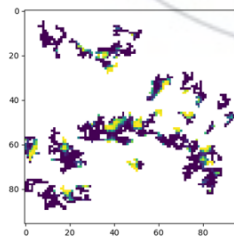
Go-Seong / 2018.03.28 / LC08_L1TP_115033_20180331_20180405_01_T1



Go-Ryeong / 2011.03.30 / LT05_L1TP_115035_20110413_20161209_01_T1



Sam-Cheok / 2017.05.06 / LC08_L1TP_114034_20170508_20170515_01_T1



Ye-Cheon / 2011.04.01 / LT05_L1TP_115035_20110413_20161209_01_T1

Figure 7. Masking images and histograms for ‘Ambiguous’

We also selected 20 predictions from 48 regions of testing and calculated the monthly average prediction accuracy. Forest fire occurred mainly from April to June, and the U-net model showed an estimated accuracy of about 93% in April and June. And in March, the prediction accuracy is low and in October, it is high, but since the number of cases is 1, making it is difficult to generalize the accuracy for the month. We also quantitatively verified the performance of the model through the verification indices of the detection type data: Proportion Correct (PC) [Kubo et al., 2017], Probability of Detection (POD), False Alarm Ratio (FAR) and Critical Access Index (CSI) [Kubo et al., 2017; Roebber, 2009]. The confusion matrix classifies pixels as A (Hit) if the model predicted correctly, B (False alarm) if the model is predicted as damaged area but is actually non-damaged area, C (Misses) if the model predicted as non-damaged area, but is actually damaged area and D (Correct negative) if the non-damaged area is predicted correctly (Table 5).

Table 5. Confusion matrix to compare the prediction and true values to measure the prediction performance of the model.

		True (Label)		Total
		Yes	No	
Predict	Yes	A (hit)	B (False alarms)	A+B
	No	C (misses)	D (Correct negative)	C+D
	Total	A+C	B+C	A + B + C + D

$$\textit{Proportion Correct (PC)} = \frac{(A+D)}{(A+B+C+D)} \quad (7)$$

$$\textit{Probability of Detection (POD)} = \frac{A}{(A+C)} \quad (8)$$

$$\textit{False Alarm Ratio (FAR)} = \frac{B}{(A+B)} \quad (9)$$

PC represents the proportion of the total number of pixels that correctly predicted both damaged and non-damaged area correctly. It is the same formula to calculate the accuracy used in this study (Equation 7). POD represents the ratio of pixels predicted to be damaged area that are actually aligned and closer to 1 is ideal (Equation 8). FAR is not actually damaged area, but it is the percentage predicted as damaged area, and the closer the value is to 1, the worse the prediction (Equation 9).

The U-net used in this study also showed high PC and POD and low FAR. In addition, the distribution of accuracy for 46 cases between April and June, excluding 1 case in March and October, showed similar accuracy, and therefore, for springtime images with frequent forest fire, the U-net model can detect damaged areas with high accuracy (Table 6).

Table 6. The number of monthly forest fire and calculated PC, POD, and FAR values of images used in this study.

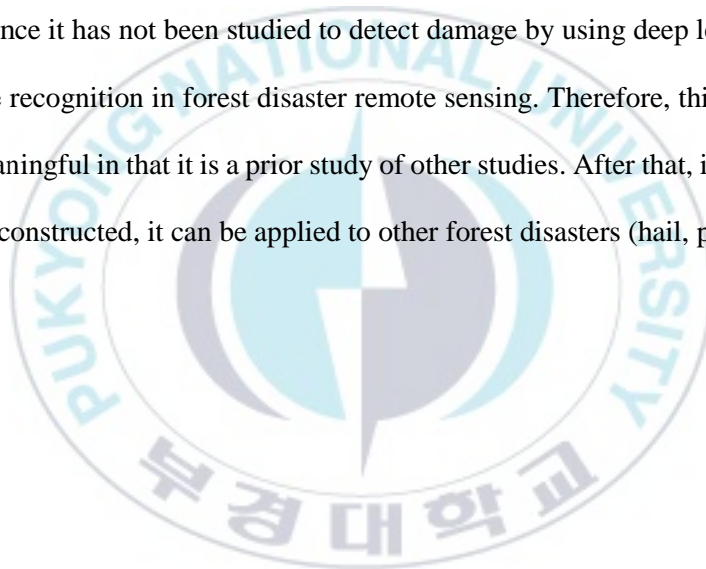
Month	Number of case	ACC(%)	PC	POD	FAR
3	1	77.23	0.77	0.35	0.12
4	14	89.2	0.89	0.62	0.26
5	23	93.93	0.94	0.72	0.29
6	9	95.38	0.95	0.81	0.28
10	1	99.11	0.99	0.95	0.18
Average		90.97	0.91	0.69	0.23

5. Conclusions

Studies that detect damaged areas based on spectral traits may effectively represent them, but the threshold setting is limited in expressing the damaged areas because it is empirical and manual. Therefore, we applied deep learning, which has superior performance compared with classical neural network and machine learning, to detect forest fire to verify the applicability and usability of satellite images and deep learning. As the image recognition model of deep learning has more label images, the model can be stably trained and learn about various samples, thereby increasing the generalization performance of the model.

In this study, it is difficult to obtain a large number of true label images, but as an alternative, we could use the data augmentation technique to improve the accuracy and generalization of the model. As a result, we achieved high average prediction accuracy of 0.892 and 0.926 for DNN classifier and U-net, respectively. Although there was a limit that the true label could not be described in details of the damaged areas due to the manual production of the true label, it was possible to predict an accuracy of about 93% even with the labels built in this study.

With more training samples and finely crafted true labels, higher and more stable predictions accuracy can be achieved, and damage ratings can be determined. In the future work, if the data is refined based on the quality assessment of the Landsat image and the noise such as the terrain occlusion are removed, the accuracy will be higher. In this study, we verified that deep learning can be applied to forest fire damage detection, and since it has not been studied to detect damage by using deep learning image recognition in forest disaster remote sensing. Therefore, this study is meaningful in that it is a prior study of other studies. After that, if a data set is constructed, it can be applied to other forest disasters (hail, pests).



6. References

1. Song, Y. S., Sohn, H. G., & Lee, S. W. (2006). Analysis of Forest Fire Damage Using LiDAR Data and SPOT-4 Satellite Images. *Journal of The Korean Society of Civil Engineers*, 26(3D), 527-534.
2. Park, S. W., Lee, S. J., Chung, C. Y., Chung, S. R., Shin, I., Jung, W. C., ... & Lee, Y. W. (2019). Satellite-based Forest Withering Index for Detection of Fire Burn Area: Its Development and Application to 2019 Kangwon Wildfires. *Korean Journal of Remote Sensing*, 35(2), 343-346.
3. Won, K. Y. (2001). Fire severity mapping using a single post-fire Landsat 7 ETM+ Imagery. *Kor J Remote Sens*, 17, 85-97.
4. Kang, J. M., Zhang, C., Park, J. K., & Kim, M. G. (2010). Forest fire damage analysis using satellite images. *Journal of the Korean Society of Surveying, Geodesy, Photogrammetry and Cartography*, 28(1), 21-28.
5. Ryu, J. H., Han, K. S., Hong, S., Park, N. W., Lee, Y. W., & Cho, J. (2018). Satellite-Based Evaluation of the Post-Fire Recovery Process from the Worst Forest Fire Case in South Korea. *Remote Sensing*, 10(6), 918. doi: 10.3390/rs10060918
6. Sunar, F., & Özkan, C. (2001). Forest fire analysis with remote sensing

- data. *International Journal of Remote Sensing*, 22(12), 2265-2277. doi: 10.1080/01431160118510
7. Won, M. S., Koo, K. S., & Lee, M. B. (2007). An quantitative analysis of severity classification and burn severity for the large forest fire areas using normalized burn ratio of Landsat imagery. *Journal of the Korean Association of Geographic Information Studies*, 10(3), 80-92.
 8. Lutz, J. A., Key, C. H., Kolden, C. A., Kane, J. T., & van Wagtenonk, J. W. (2011). Fire frequency, area burned, and severity: a quantitative approach to defining a normal fire year. *Fire Ecology*, 7(2), 51-65. doi: 10.4996/fireecology.0702051
 9. Navarro, G., Caballero, I., Silva, G., Parra, P. C., Vázquez, Á., & Caldeira, R. (2017). Evaluation of forest fire on Madeira Island using Sentinel-2A MSI imagery. *International journal of applied earth observation and geoinformation*, 58, 97-106. doi: 10.1016/j.jag.2017.02.003
 10. Lee, S., Kim, K., Kim, Y., Kim, J., & Lee, Y. (2017). Development of FBI (Fire Burn Index) for Sentinel-2 images and an experiment for detection of burned areas in Korea. *Journal of the Association of Korean Photo-Geographers*, 27(4), 187-202. doi: 10.35149/jakpg.2017.27.4.012

11. Turker, M., & San, B. T. (2003). SPOT HRV data analysis for detecting earthquake-induced changes in Izmit, Turkey. *International Journal of Remote Sensing*, 24(12), 2439-2450. doi: 10.1080/0143116031000070427
12. Park, S. W., & Lee, Y. W. (2019, October). Detection of forest disaster using high-resolution satellite images with semantic segmentation. In *Image and Signal Processing for Remote Sensing XXV* (Vol. 11155, p. 111551R). International Society for Optics and Photonics. doi: 10.1117/12.2532990
13. Long, J., Shelhamer, E., & Darrell, T. (2015). Fully convolutional networks for semantic segmentation. In *Proceedings of the IEEE conference on computer vision and pattern recognition* (pp. 3431-3440). doi: 10.1109/cvpr.2015.7298965
14. Song, A., Choi, J., Han, Y., & Kim, Y. (2018). Change detection in hyperspectral images using recurrent 3d fully convolutional networks. *Remote Sensing*, 10(11), 1827. doi: 10.3390/rs10111827
15. Kussul, N., Lavreniuk, M., Skakun, S., & Shelestov, A. (2017). Deep learning classification of land cover and crop types using remote sensing data. *IEEE Geoscience and Remote Sensing Letters*, 14(5), 778-782. doi: 10.1109/lgrs.2017.2681128
16. Zhang, F., Du, B., & Zhang, L. (2015). Scene classification via a

- gradient boosting random convolutional network framework. *IEEE Transactions on Geoscience and Remote Sensing*, 54(3), 1793-1802. doi: 10.1109/tgrs.2015.2488681
17. Kim, S., Lee, W., Park, Y. S., Lee, H. W., & Lee, Y. T. (2016, December). Forest fire monitoring system based on aerial image. In 2016 3rd International Conference on Information and Communication Technologies for Disaster Management (ICT-DM) (pp. 1-6). IEEE. doi: 10.1109/ict-dm.2016.7857214
18. Masek, J. G., Vermote, E. F., Saleous, N. E., Wolfe, R., Hall, F. G., Huemmrich, K. F., ... & Lim, T. K. (2006). A Landsat surface reflectance dataset for North America, 1990-2000. *IEEE Geoscience and Remote Sensing Letters*, 3(1), 68-72, doi: 10.1109/lgrs.2005.857030
19. Vermote, E., Justice, C., Claverie, M., & Franch, B. (2016). Preliminary analysis of the performance of the Landsat 8/OLI land surface reflectance product. *Remote Sensing of Environment*, 185, 46-56. doi: 10.1016/j.rse.2016.04.008
20. Roy, D. P., Wulder, M. A., Loveland, T. R., Woodcock, C. E., Allen, R. G., Anderson, M. C., ... & Scambos, T. A. (2014). Landsat-8: Science and product vision for terrestrial global change research. *Remote sensing of Environment*, 145, 154-172. doi:

10.1016/j.rse.2014.02.001

21. Najafabadi, M. M., Villanustre, F., Khoshgoftaar, T. M., Seliya, N., Wald, R., & Muharemagic, E. (2015). Deep learning applications and challenges in big data analytics. *Journal of Big Data*, 2(1), 1. doi: 10.1186/s40537-014-0007-7
22. LeCun, Y., Bengio, Y., & Hinton, G. (2015). Deep learning. *nature*, 521(7553), 436-444. doi: 10.1038/nature14539
23. Kumar, L., Schmidt, K., Dury, S., & Skidmore, A. (2002). Imaging spectrometry and vegetation science. In *Imaging spectrometry* (pp. 111-155). Springer, Dordrecht. doi: 10.1007/0-306-47578-2_5
24. Miller, J. D., & Thode, A. E. (2007). Quantifying burn severity in a heterogeneous landscape with a relative version of the delta Normalized Burn Ratio (dNBR). *Remote Sensing of Environment*, 109(1), 66-80. doi: 10.1016/j.rse.2006.12.006
25. Lee, J. M., Won, M. S., Lim, J. H., & Lee, S. W. (2012). Effects of Edge Area and Burn Severity on Early Vegetation Regeneration in Damaged Area. *Journal of Korean Society of Forest Science*, 101(1), 121-129.
26. Szegedy, C., Toshev, A., & Erhan, D. (2013). Deep neural networks for object detection. In *Advances in neural information processing systems* (pp. 2553-2561).

27. Bengio, Y., Courville, A., & Vincent, P. (2013). Representation learning: A review and new perspectives. *IEEE transactions on pattern analysis and machine intelligence*, 35(8), 1798-1828. doi: 10.1109/tpami.2013.50
28. Brownlee, J. (2018). *Better Deep Learning: Train Faster, Reduce Overfitting, and Make Better Predictions*. Machine Learning Mastery.
29. Ronneberger, O., Fischer, P., & Brox, T. (2015, October). U-net: Convolutional networks for biomedical image segmentation. In *International Conference on Medical image computing and computer-assisted intervention* (pp. 234-241). Springer, Cham. doi: 10.1007/978-3-319-24574-4_28
30. Kim, Y. (2014). Convolutional neural networks for sentence classification. arXiv preprint arXiv:1408.5882. doi: 10.3115/v1/d14-1181
31. Krizhevsky, A., Sutskever, I., & Hinton, G. E. (2012). Imagenet classification with deep convolutional neural networks. In *Advances in neural information processing systems* (pp. 1097-1105). doi: 10.1145/3065386
32. Simonyan, K., & Zisserman, A. (2014). Very deep convolutional networks for large-scale image recognition. arXiv preprint arXiv:1409.1556.

33. Szegedy, C., Liu, W., Jia, Y., Sermanet, P., Reed, S., Anguelov, D., ... & Rabinovich, A. (2015). Going deeper with convolutions. In Proceedings of the IEEE conference on computer vision and pattern recognition (pp. 1-9). doi: 10.1109/cvpr.2015.7298594
34. He, K., Zhang, X., Ren, S., & Sun, J. (2016). Deep residual learning for image recognition. In Proceedings of the IEEE conference on computer vision and pattern recognition (pp. 770-778). doi: 10.1109/cvpr.2016.90
35. Noh, H., Hong, S., & Han, B. (2015). Learning deconvolution network for semantic segmentation. In Proceedings of the IEEE international conference on computer vision (pp. 1520-1528). doi: 10.1109/iccv.2015.178
36. Pappagari, R., Villalba, J., & Dehak, N. (2018, April). Joint Verification-Identification in end-to-end Multi-Scale CNN Framework for Topic Identification. In 2018 IEEE International Conference on Acoustics, Speech and Signal Processing (ICASSP) (pp. 6199-6203). IEEE. doi: 10.1109/icassp.2018.8461673
37. Wang, X., Shrivastava, A., & Gupta, A. (2017). A-fast-rcnn: Hard positive generation via adversary for object detection. In Proceedings of the IEEE Conference on Computer Vision and Pattern Recognition (pp. 2606-2615). doi: 10.1109/cvpr.2017.324

38. Lim, H. K., Kim, J. B., Kwon, D. H., & Han, Y. H. (2017). Comparison Analysis of TensorFlow's Optimizer Based on MNIST's CNN Model. *Journal of Advanced Technology Research*, 2(1), 6-14.
39. Kingma, D. P., & Ba, J. (2014). Adam: A method for stochastic optimization. arXiv preprint arXiv:1412.6980.
40. Nair, V., & Hinton, G. E. (2010). Rectified linear units improve restricted boltzmann machines. In *Proceedings of the 27th international conference on machine learning (ICML-10)* (pp. 807-814).
41. Candel, A., Parmar, V., LeDell, E., & Arora, A. (2016). Deep learning with H2O. H2O. ai Inc.
42. Yang, X., Lo, D., Xia, X., Zhang, Y., & Sun, J. (2015, August). Deep learning for just-in-time defect prediction. In *2015 IEEE International Conference on Software Quality, Reliability and Security* (pp. 17-26). IEEE. doi: 10.1109/qrs.2015.14
43. Mesnil, G., Dauphin, Y., Glorot, X., Rifai, S., Bengio, Y., Goodfellow, I., ... & Vincent, P. (2011, July). Unsupervised and transfer learning challenge: a deep learning approach. In *Proceedings of the 2011 International Conference on Unsupervised and Transfer Learning workshop-Volume 27* (pp. 97-111). JMLR. org.
44. Kubo, Y., Den, M., & Ishii, M. (2017). Verification of operational solar flare forecast: Case of Regional Warning Center Japan. *Journal of*

Space Weather and Space Climate, 7, A20. doi: 10.1051/swsc/2017018

45. Roebber, P. J. (2009). Visualizing multiple measures of forecast quality. *Weather and Forecasting*, 24(2), 601-608. doi: 10.1175/2008waf2222159



This is the final page of a Thesis/Dissertation and should be a blank page

